Chemical Physics Letters 858 (2025) 141740

Contents lists available at ScienceDirect

Chemical Physics Letters

journal homepage: www.elsevier.com/locate/cplett

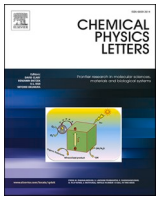

On the electronic properties of a pH-responsive molecular thread for H-shaped molecular shuttles in aqueous solution

Costantino Zazza [a,*], Nico Sanna [a,b], Stefano Borocci [a,c], Felice Grandinetti [a,c]

[a] Department for Innovation in Biological, Agro-food and Forest systems, Università della Tuscia (DIBAF), L.go dell'Università, s.n.c., 01100 Viterbo, Italy
[b] CNR-ISTP (Istituto per la Scienza e Tecnologia dei Plasmi), Via G. Amendola 122/D, 70126 Bari, Italy
[c] Istituto per i Sistemi Biologici del CNR (ISB), Sede di Roma - Meccanismi di, Reazione c/o Dipartimento di Chimica, Sapienza Università di Roma, P.le A. Moro 5, 00185 Rome, Italy

A B S T R A C T

A molecular thread composed by Tolyl-Viologen-Phenylene-Imidazole (**T-VPI**) subunits is investigated in a neutral aqueous environment and under acid conditions (**T-VPI-H**$^+$) by classical molecular dynamics and a hybrid quantum mechanical/molecular mechanics approach. Nanosolvation patterns and UV/Vis spectroscopic properties for both **T-VPI** and **T-VPI-H**$^+$ synthetic systems are characterized by analysing classical configurations with a QM(TD-DFT)/MM+C-PCM decomposition model. The derived aqueous UV/Vis absorptions support experimental observations under equilibrium conditions at 298 K while shedding light on the electronic degrees of freedom involved in the electronic excitations.

1. Introduction

The progress of our civilization has always been associated with our capability to realize machines of increasing complexity and specific functionalities. Clearly, with the developments in miniaturization techniques we have observed the appearance of nanoscale-size machines and devices within dimensions in line with those of molecular aggregates.[1–3] In analogy with machines of macroscopic sizes, a molecular-level machine has been defined as "an assembly of a distinct number of molecular components that are designed to perform machine-like movements (output) as a result of an appropriate external stimulation (input)". The external perturbation can typically be provided by several sources like for example: chemical reactions, pH-variation, electrochemical reduction/oxidation, light radiations. [4–9] Biological molecular machines in cells such as ATP synthase, [10–12] Titin [13,14] or Myosin [15–17] work efficiently, under physiological conditions, promoting mechanical movements in living organisms. These proteins are far more complex than any other molecular machines that have yet been artificially constructed. However, in analogy with biological systems, synthetic molecular motors with stimuli-responsive controllable conformational changes of increasing complexity in different environments are emerging in literature.[18–25] In this context, our attention has been drawn to a recently released aqueous pH and metal-actuated synthetic molecular shuttle in which the reversible coexistence of translational isomers results finely modulated by acidic conditions or by a gradual ratio of Ag^+ cations. [26] In more detail, a cucurbit[7]uril (**CB**[7]) macrocycle on a Tolyl-Viologen-Phenylene-Imidazole (**T-VPI**) molecular wire – at neutral or acid pH (**T-VPI-H**$^+$) or even after Ag^+ addition (**T-VPI-Ag**$^+$) – is able to reversibly complex both **T** and **P** functional subunits contrary to what had been observed on similar systems in dilute water solution (see Scheme 1). [26] Always remaining in this context, taking as a reference condition the deposited crystallographic structure (CCDC:2217466) [26] featuring a host(**CB**[7]):guest (**T-VPI-Ag**$^+$) ratio equal to 2:1, we investigated the nature of the chemical interactions characterizing the complexation of the **CB**[7] macrocycle over **T** and **P** stations by combining DFT-based converged electronic wavefunctions with the Quantum Theory of Atoms in Molecules (QTAIM) decomposition analysis. [27] The results obtained – only considering the investigated systems in their own electronic ground state – provide useful insights on the overall ensemble of supramolecular interactions driving discretional complexations and pH-responsive translational movements in a not-interlocked molecular shuttle.

In this contribution, always taking direct inspiration from the work proposed by A. Kriat et.al., [26] we computationally addressed the UV–VIS spectroscopic properties of **T-VPI** and **T-VPI-H**$^+$ molecular thread in water dilute solution at room temperature. More specifically, we combined Quantum-Mechanics (QM) and classical Molecular Dynamics (MD) techniques so to realize, at atomistic level, the effects of nanosolvation patterns driven by thermal fluctuations at the thread/water interface on the electronic degrees of freedom involved in the

* Corresponding author.
E-mail address: costantino.zazza@unitus.it (C. Zazza).

https://doi.org/10.1016/j.cplett.2024.141740
Received 12 September 2024; Received in revised form 25 October 2024; Accepted 4 November 2024
Available online 6 November 2024

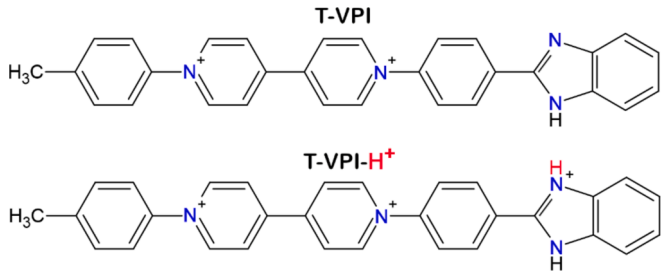

Scheme 1. . Chemical structure of **T-VPI** (upper panel) and **T-VPI-H**$^+$ (lower panel) synthetic molecular threads in water dilute solution at neutral and acidic conditions. These molecular systems are composed of 4 different groups or "stations" in the case of the presence of an encircling macrocycle; from left to right: Tolyl (**T**), Viologen (**V**), Phenylene (**P**) and Imidazole (**I** or **I-H**$^+$).

excitation processes detected in the laboratory. Our investigation analytically shows – for the first time – that the most prominent signals in the UV–Vis absorption spectra of **T-VPI** and **T-VPI-H**$^+$ in H_2O should be ascribed to valence $^1\pi \rightarrow \pi^*$ electronic excitations also showing in some cases a charge-transfer (C-T) character among different functional groups. Also, we observe an intricate balance between electronic properties and solvation dynamics which should plausibly affect complexation pathways along the investigated synthetic threads.

2. Computational details

The molecular systems depicted in Scheme 1 were optimized at DFT level [28] adopting the popular hybrid exchange–correlation Becke 3-parameters Lee–Yang–Parr (B3LYP) functional, [29–31] its Coulomb-attenuated formulation (CAM-B3LYP) [32] and the PBE0 functional mixing the Perdew–Burke-Ernzerhof (PBE) exchange energy and Hartree–Fock (HF) exchange energy in a set 3:1 ratio, along with the full PBE correlation energy. [33] We used as starting coordinates those extracted from X-Ray structure; the 6–311+G** basis set [34] was applied for all the atoms in conjunction with the Grimme's dispersion D3 damping scheme. [35] The investigated molecular threads were relaxed by applying a redundant-based internal coordinates algorithm [36] in solution mimicking the hosting dilute solution environment by the Conductor-like Polarizable Continuum Model (C-PCM) [37] as implemented in the Gaussian code (Rev. C01). [38].

Local reactivity descriptors for the two investigated molecular threads are also addressed in the field of the Conceptual DFT (CDFT) framework. [39] In particular, we have characterized electrophilic and nucleophilic regions potentially prone to complexation pathways by using the empirically defined Orbital-Weighted Fukui functions [$f_w^-(\boldsymbol{r})$ and $f_w^+(\boldsymbol{r})$] [40] as defined by the following expressions:

$$f_w^-(\boldsymbol{r}) = \sum_{i}^{HOMO} w_i \rho_i(\boldsymbol{r}); f_w^+(\boldsymbol{r}) = \sum_{LUMO}^{\infty} w_i \rho_i(\boldsymbol{r})$$

in which w_i are the so-called weighting factors, $\rho_i(\boldsymbol{r})$ represents the square of the *i*-th molecular orbital and the term *i* runs over a set of MOs. The w_i terms are defined – for both the $f_w^-(\boldsymbol{r})$ and $f_w^+(\boldsymbol{r})$ functions – according to the Gaussian ansatz as follows:

$$w_i = \frac{\exp\left[-\left(\frac{\mu-\epsilon_i}{\Delta}\right)^2\right]}{\sum_i^{HOMO}\exp\left[-\left(\frac{\mu-\epsilon_i}{\Delta}\right)^2\right]}; w_i = \frac{\exp\left[-\left(\frac{\mu-\epsilon_i}{\Delta}\right)^2\right]}{\sum_{LUMO}^{\infty}\exp\left[-\left(\frac{\mu-\epsilon_i}{\Delta}\right)^2\right]}$$

where μ is the chemical potential – approximately estimated as $(E_{HOMO} + E_{LUMO})/2$ – ϵ_i the energy of each molecular orbital and Δ represents the width of a Gaussian-type function determining the energy range for orbitals that make a substantial contribution to the reactivity. A Gaussian model was chosen, as a matter of convenience, because the numbers of molecular orbitals and its relative contribution to reactivity can be controlled with a single parameter, Δ, typically set as first guess to 0.1 Hartree. [40] We applied the formulations reported above to closed-shell single-determinant wavefunctions and the computations are done with the Multiwfn program (version 3.8.dev) [41]; in this context, we do not consider diffuse functions to avoid spurious effects in the definition of $f_w^-(\boldsymbol{r})$ and $f_w^+(\boldsymbol{r})$ functions.

Furthermore, in order to refine – from a dynamical point of view – the lowest valence UV/Vis absorption bands experimentally detected in neutral and acidic conditions at 298 K in H_2O, we have used a Time-Dependent (TD) approach [42] over a QM/MM/C-PCM partitioning scheme as already applied over similar systems. [19,21,23,25] In this respect, we extracted from an MD trajectory of 400 ns for both **T-VPI** and **T-VPI-H**$^+$ in H_2O a snapshot every 20.0 ns, corresponding to 20 evenly spaced configurations. We also remark that position restraints – with a force constant of 10^5 kJ·mol^{-1}·nm^{-2} – are applied on each of the thread atoms so as to rule out solute dynamical effects. Each MD sampling was started considering the synthetic thread at the centre of a cubic box of 44 Å; afterwards, water molecules were introduced in the simulation box using the Single Point Charge (SPC/E) model [43]. These solutes result then confined within 20 different spherical nanodroplets in interaction with the solvent treated both by explicit molecules (treated at QM level or as atomic point charges) and implicit ones (*i.e.*, a spherical C-PCM cavity, see Fig. 1). In this respect, a subset of water molecules featuring H-bonding contacts with the synthetic solutes were treated at QM level within the proposed QM/MM/C-PCM approach. These interactions are essentially based on two cutoffs: *i)* the Acceptor-Donor-Hydrogen (Ac–Dn–H) angle between the three atoms involved in the H-bond; *j)* the distance between the two heavy atoms involved in the interaction (Ac–Dn). The applied criteria we selected are: Ac–Dn–H angle $\leq 30°$ and Ac–Dn distance ≤ 3.5 Å. [23] The OPLS All-Atom Force Field parameters [44] were adopted for the two investigated threads. MD simulations were performed using GROMACS Software (release 2022.6) [45].

3. Results and discussion

The structures of the **T-VPI** and **T-VPI-H**$^+$ molecular threads were optimized at C-PCM(H_2O)/[B3LYP/CAM-B3LYP/PBE0](D3)/6–311+G** level of theory and the applied DFT functionals show only very small changes in the optimized structural parameters (< 3 %). As for the low-lying vertical excitations (data displayed in Fig. 2), the B3LYP and PBE0 functionals provide similar excitation patterns both in terms of excitation wavelengths and oscillator strengths. On the other hand, at C-PCM/CAM-B3LYP(D3)/6–311+G** level of computation we obtained UV/Vis absorption spectra closer to the experimental findings. [26] As a matter of fact, in water dilute solution, the main absorption bands of the **T-VPI** system centred at around 350 and 290 nm result well reproduced with absorptions falling at 337 (oscillator strength, *f*, equal to 0.80) and 278 nm with the latter arising from the convolution of two signals lying at 274 ($f = 0.61$) and 295 nm ($f = 0.37$). The other two DFT functionals tend to overestimate the UV/Vis signal experimentally recorded at 350 nm actually providing values lying at around 400 nm ($f = 0.38$; B3LYP) and 385 nm ($f = 0.40$; PBE0). Moreover, our computations indicate that these absorption bands mirror a valence $^1\pi \rightarrow \pi^*$ character involving in some cases molecular orbitals localized over specific functional subunits. As a matter of fact, taking into consideration the aqueous **T-VPI** species with the CAM-B3LYP functional, we observe that the first excitation at 337 nm mainly shows a HOMO → LUMO(80 %) composition characterized by an intramolecular charge-transfer process from the **I**midazole subunit towards the remaining part of the molecular skeleton, see the molecular orbitals depicted in Fig. 3. Always remaining in this context, the electronic excitation at 295 nm presents a HOMO-2 → LUMO(83 %) singlet excitation while the signal at 274 nm display a multiple electronic excitation character [*i.e.*, HOMO → LUMO+1(26 %);HOMO → LUMO+4(56 %)]. Interestingly we observe that, the HOMO-2 orbital results essentially widespread over the **T**olyl + **V**iologen moieties while the virtual orbitals (LUMO+1 and

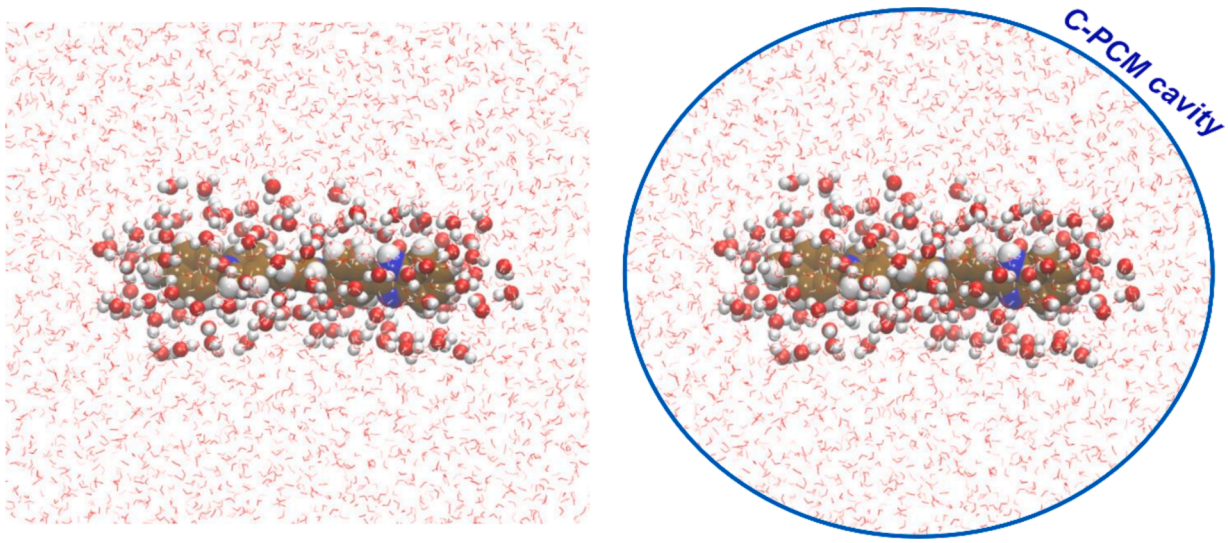

Fig. 1. Left panel: the MD simulation box with the **T-VPI** (or **T-VPI-H**$^{+}$) thread surrounded by explicit solvent molecules; water molecules at the solute/solvent interface are highlighted using the van der Waals drawing method in VMD. Right panel: a spherical QM/MM/C-PCM aqueous nanodroplet as extracted from the MD simulation. Water molecules selected within the QM layer are those found in H-bond contact with the solute by using the "gmx hbond" module as proposed in the Gromacs software.

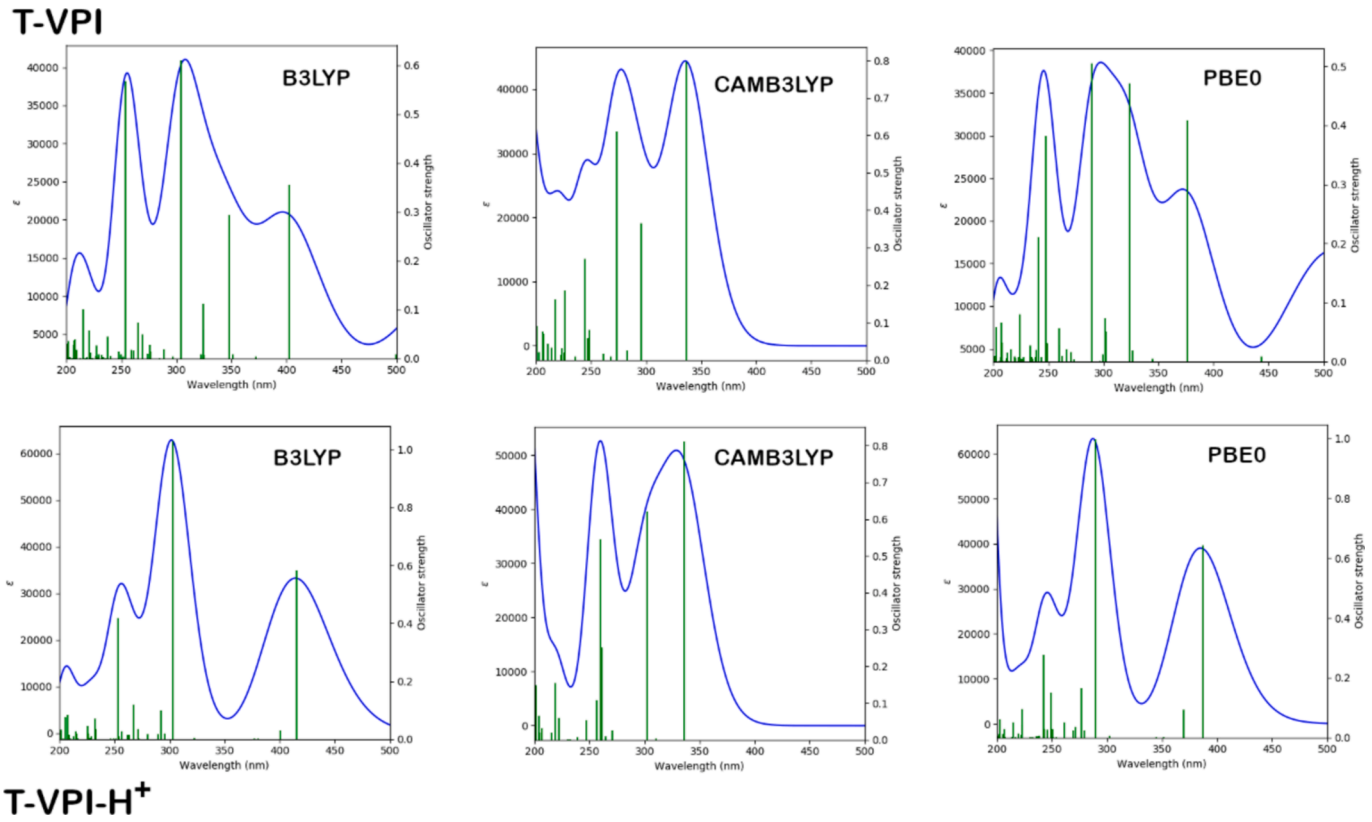

Fig. 2. Upper panel: UV/Vis absorption spectra (ε in L·mol^{-1}·cm^{-1}) from optimized **T-VPI** molecular thread at C-PCM/[B3LYP//CAM-B3LYP//PBE0](D3)/6–311+G** level of theory in dilute water environment. Lower panel: same spectroscopic data from **T-VPI-H**$^{+}$. The molecular orbitals responsible for the main absorption signals in the range 200–500 nm are also displayed in Fig. 3.

LUMO+4) features a π* character distributed over the entire **T-VPI** system. We also observe other two electronic excitations at shorter wavelengths, 244 ($f = 0.26$) and 226 ($f = 0.19$) nm, with the following composition: HOMO-5 → LUMO(54 %) and HOMO-10 → LUMO(16 %); HOMO-10 → LUMO(31 %), HOMO → LUMO+1(27 %), HOMO → LUMO+4(14 %). Regarding the stable form in acidic condition, we have that the aqueous **T-VPI-H**$^{+}$ thread also reports TD-DFT excitations in agreement with experimental findings. As a matter of fact, A. Kriat at.al. [26] clearly detected that the protonation of the **I** moiety in water dilute solution is correlated with a slight blue shift of the UV/Vis absorption spectra while passing from **T-VPI** to **T-VIP-H**$^{+}$. This trend is actually appreciated by our simulations – at C-PCM/CAM-B3LYP(D3)/

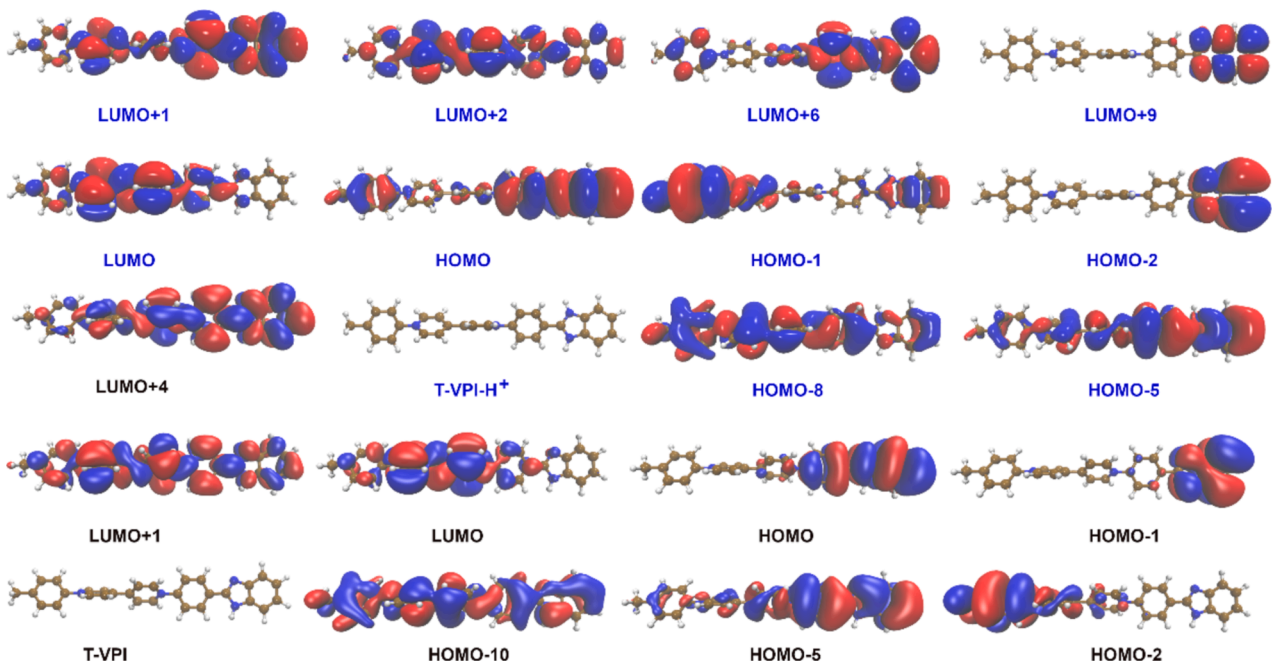

Fig. 3. **T-VPI** and **T-VPI-H**$^+$ molecular orbitals – as extracted at C-PCM(H_2O)/CAM-B3LYP(D3)/6–311+G** level of theory – involved in the electronic excitations depicted in Fig. 2 featuring oscillator strengths > 0.2; the blue colour reflects the positive (+) counterpart of the corresponding eigenvector and an isodensity surface plot value of 0.015 $e{\cdot}a_0^3$ is represented.

6–311+G** level – has shown in Fig. 2. The UV/Vis spectra that has emerged results composed by a lowest $\pi \rightarrow \pi^*$ band with a $\lambda_{max} \approx$ 327 nm and a shoulder at ≈305 nm mainly arising from the overlap of two singlet electronic transitions falling at 336 ($f = 0.81$) and 302 ($f = 0.62$) nm; the first transition substantially involves a HOMO → LUMO(78 %) excitation while the second signal a HOMO-2 → LUMO (83 %) composition. Moreover, the singlet electronic excitation at 260 ($f = 0.55$) nm also presents a $\pi \rightarrow \pi^*$ character with basically a HOMO → LUMO+1 (56 %) transition. The experimental absorption profile for the aqueous **T-VPI-H**$^+$ display a broad band with a $\lambda_{max} \approx$ 340 nm and a shoulder at 300 nm; our simulations while reproducing well this pattern provide additional information regarding the electronic degrees of freedoms responsible for the absorption of light.

It is worth to note that both B3LYP and PBE0 functional – as already observed before – tends to overestimate the lowest energy absorption band [26] while providing reasonable results at around 300 nm (see Fig. 2). At last, we would like to mention that other three signals – at TD/CAM-B3LYP – are detected in the range 250–180 nm: *i)* a signal at 232 nm ($f = 0.55$) mainly arising from HOMO-8 → LUMO(40 %), HOMO-5 → LUMO(28 %) and HOMO → LUMO(21 %) single electronic excitation characters; *ii)* an excitation at 211 nm ($f = 0.19$) composed by HOMO-8 → LUMO(21 %), HOMO-5 → LUMO(22 %) and HOMO-2 → LUMO+9 (14 %) excitations; *iii)* a signal at 198 nm with $f = 0.14$ and the composition: HOMO-1 → LUMO+2(36 %), HOMO-1 → LUMO+1(25 %), HOMO → LUMO+6(18 %). All these bands with an $f > 0.12$ feature a valence $^1\pi \rightarrow \pi^*$ character as clearly shown in Fig. 3.

Table 1
. Estimated fragment (**T**, **V**, **P**, **I** or **I-H**$^+$) charges via atomic dipole moment corrected Hirshfeld population methodology,[41] at CAM-B3LYP/(D3)/6–311+G** level of theory – for **T-VPI** and **T-VPI-H**$^+$ threads in water dilute solution modelled via C-PCM algorithm (see Section 2).

Fragment	T-VPI	T-VPI-H$^+$
Tolyl-	+0.26	+0.26
Viologen-	+1.49	+1.53
Phenyl-	+0.22	+0.33
Imidazole **or I-H**$^+$	+0.03	+0.88
Total	+2.00	+3.00

Table 1 shows the estimated fragment charges for both the investigated threads with the implicit C-PCM solvent model. This analysis allows us to estimate the atomic charge distribution in a molecular system from converged electronic wavefunctions. As expected, the most relevant positive charge is localized over the **V**iologen group (+1.49 in the **T-VPI** and + 1.53 in the **T-VPI-H**$^+$) followed by the **I**midazole moiety featuring a value of + 0.88 upon protonation (in the neutral species this fragment is substantially quasi-neutral with an associated charge of + 0.03). The **P**henyl group close to **I** also increases its local charge (from + 0.22 to + 0.33) while the **T**olyl moiety results substantially unaltered (+0.26). Moreover, in Fig. 4 we report the plot of the Orbital-Weighted Fukui functions [$f_w^-(\boldsymbol{r})$ and $f_w^+(\boldsymbol{r})$] according to their mathematical definition reported in section 2. [40] Looking at this figure, we immediately realize that, in the case of the **T-VPI** thread, the unsaturated nitrogen atom of the **I** group presents – in the $f_w^-(\boldsymbol{r})$ – the most relevant value for an electrophilic attack; a local value of $f_w^-(\boldsymbol{r}) = 0.090$ justifies the observed reactivity *in silico* upon acidification of the aqueous solution or addition of Ag^+ ions. [26] Always considering the **T-VPI** thread, the $f_w^+(\boldsymbol{r})$ distribution is mainly located – in agreement with the data reported in Table 1- on the **V**iologen moiety which therefore results prone to a nucleophilic attack or complexation. The estimated $f_w^+(\boldsymbol{r})$ values at atomic scale are found in the 0.043–0.063 range thus suggesting that such a moiety is plausibly expected to play a key role in the observed supramolecular complexation in the presence of a lone pairs electron-rich **CB**[7] macrocycle. [26] The **T-VPI-H**$^+$ thread instead shows that **T**olyl and **I**midazole moieties might result particularly appealing for an electrophilic attack with their π electrons while the **V**iologen group still features the largest reactivity towards nucleophilic species in water dilute solution.

At last, with the target of theoretically modelling the lowest UV/Vis absorption pathways of the two investigated forms of such a thread between 200–500 nm in water at room temperature, we introduce a QM/MM/C-PCM partitioning scheme. In the QM region, we have properly considered **T-VPI** and **T-VPI-H**$^+$ within their optimized structures at C-PCM/CAM-B3LYP(D3)/6–311+G** level (see Fig. 4). These structures were then embedded within a classical simulation box and a

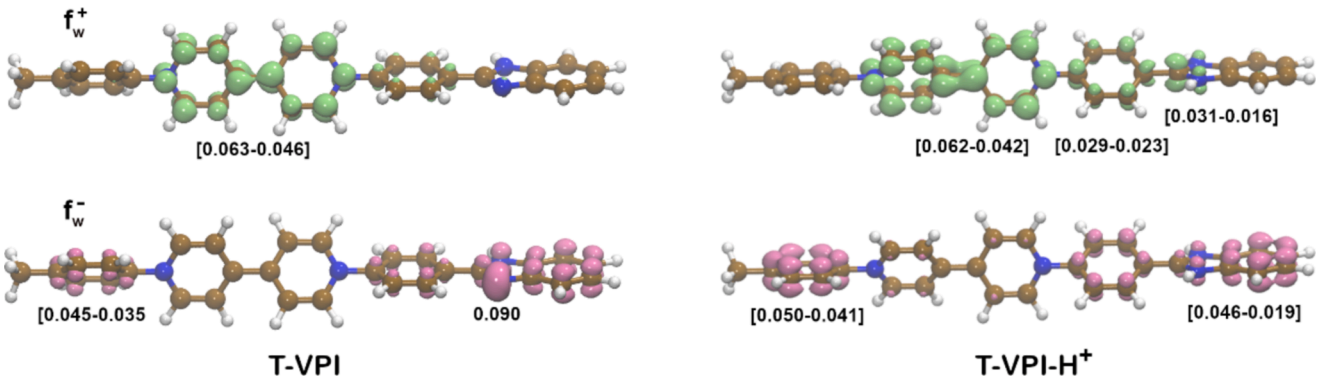

Fig. 4. Orbital-Weighted Fukui functions, $f^{+}_{w}(\mathbf{r})$ in green and $f^{-}_{w}(\mathbf{r})$ in magenta, of the two investigated **T-VPI** (left panel) and **T-VPI-H**$^{+}$(right panel) synthetic molecular threads obtained at the C-PCM(H_2O)/CAM-B3LYP/(D3)/6-311G** level of theory.

MD trajectory of 400 ns in water at 298 K was sampled. Afterwards, the classical trajectories were analyzed extracting a frame every 20 ns. These subsets of uncorrelated 20 + 20 (evenly spaced) configurations are then used to build up nanodroplets with spherical shapes (see Section 2 for major details). In this respect, the absorption properties for both the forms of this thread are obtained by combining QM [CAM-B3LYP(D3)]/6–311+G**)/MM/C-PCM excitation wavelengths with oscillator strengths and using gaussian broadening functions having a full width at half maximum (FWHM) of 20 nm. The convoluted adsorptions that have emerged are shown in Fig. 5a (**T-VPI** + H_2O) and 5b (**T-VPI-H**$^{+}$ + H_2O). In neutral conditions, we have that the convoluted UV/Vis absorption spectrum features two single peak profiles in the range 200 − 500 nm with λ_{max} falling at 344 nm (λ_{exp}≈350 nm) and 279 nm (λ_{exp}≈290 nm). Interestingly, we observe that nanosolvation patterns driven by thermal fluctuations and non-covalent interactions finely modulates the spectroscopic properties of **T-VPI** in aqueous environment. The lowest $^{1}\pi \rightarrow \pi^{*}$ energy band lying at almost 344 nm – computed QM [CAM-B3LYP(D3)]/6–311+G**)/MM/C-PCM level – features excitation wavelengths spanning a spectral region from 333 to 356 nm with an average value of 346 nm and a standard deviation of 6 nm. The corresponding oscillator strengths result as well tuned by solvation effects, spanning values between 0.77 and 0.91. A similar modulation has been also observed in the excitation band showing a λ_{max}≈279 nm (excitation wavelengths in the range 273–281 nm with *f* between 0.58–0.79); this band is further reinforced by another absorption detected at around 253 nm with *f*≈0.3. Our computations then reveal that nanosolvation dynamics at finite-temperature conditions coupled with non-covalent interactions treated at QM and/or MM level can affect the UV/Vis spectroscopic observables of such a synthetic thread. Furthermore, the slight shifts observed are in line with the main $^{1}\pi \rightarrow \pi^{*}$ character of the most intense excitations which do not include a drastic rearrangement of the electronic density during the absorption of light. Finally, we would like to point out that accordingly to the imposed geometrical parameters (cutoff angle ≤ 30° and distance ≤ 3.5 Å) QM-based solvation effects are ascribed to H-bond interactions between water molecules and the **I**midazole subunit (see the inset of Fig. 5a); the water density maps around the **I** group are calculated using the positions of either oxygen or hydrogen atoms of the water molecules along the MD sampling of 400 ns at 298 K; these maps reveal the presence of well-structured first hydration layers encircling such a group in proximity of the amine-hydrogen, the opposite nitrogen atom and the region encircling the five membered ring. Some peculiar features have been pointed out by inspection of the radial distribution functions (RDFs). The solvent distribution around the amine-hydrogen atom shows a first solvation shell with a maximum [R_{max}(*N-H–O*$_W$)] at around 2.0 Å and an extension up to 2.5 Å. The coordination number arising from the numerical integration of the first main peak suggests the presence of a single water molecule in electrostatic interaction with the amine-hydrogen atom. The remaining first hydration shell encircling the N atom, and the five membered ring features a R_{max}(*N–O*$_W$) intermolecular distance peaked at around 3.3 Å with an extension up to 4.4 Å and a coordination number of ~4 water molecules. In this imposed QM/MM/

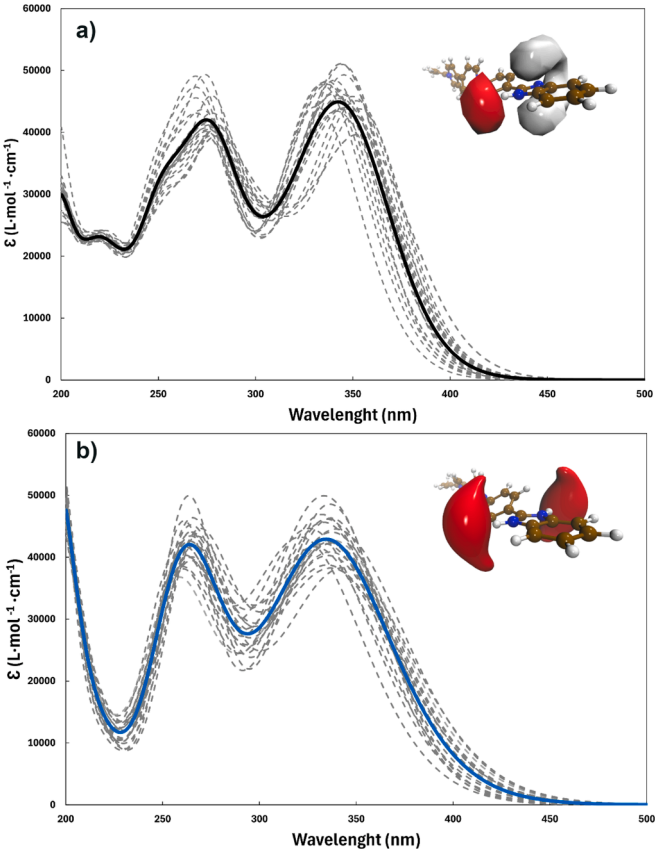

Fig. 5. A) **T-VPI** UV/Vis absorption spectra – black solid line at [CAM-B3LYP (D3)/6–311+G**/MM + C-PCM] level – in H_2O at 298 K. We considered 20 equally spaced MD (400 ns at 298 K, grey dashed lines) frames, and the electronic excitations are computed using spherical aqueous nanodroplets; the thread – at the centre of this cavity – interacts with explicit water molecules treated at QM level if found in H-bond contact or as simple Atomic Point Charges (see Section 2). Bulk solvation effects are considered within the C-PCM decomposition. In the inset we show the water density regions (O in red, H in light grey) featuring solvent molecules in H-bond contact with the solute. b) **T-VPI-H**$^{+}$ UV/Vis absorption spectra – blue solid line – in H_2O at 298 K. In the inset the water density regions characterizing the mutual positions of water molecules forming H-bond with the solute.

C-PCM partitioning scheme the remaining water molecules are then treated as atomic point charges [43] with coordinates following those sampled with the applied MD propagator. In this context, the applied methodology strongly resembles the strategies adopted for a quantitative reproduction of the infrared (IR) spectra of hydrogen bonded systems, where additional quantization of the vibrational modes of functional groups directly involved in hydrogen-bonded bridges is necessary. [46–48] Although a detailed analysis of the effects of hydration on the normal modes of vibration of the investigated systems is not among the aims of the present research, the first hydrated cluster arising from the equilibration process shows an N-H stretching mode of the **I** species at around 3474 cm^{-1} because of the appreciated N-H···Ow interactions. In the absence of the hydrated layer, the same thread only embedded in the implicit C-PCM model features for the same mode, a frequency at 3675 cm^{-1} This trend one more time highlights that these kinds of interactions lead to significant changes in the infrared (IR) spectrum like frequency shifts and increases of IR intensities. The experimental IR spectra of protonated **I**midazole–$(water)_n$ complexes report a diagnostic N-H frequency at ≈3470 cm^{-1} following microhydration. [49].

In the same figure, panel b, we display the absorption spectra of aqueous **T-VPI-H**$^+$ which show a first band lying at 333 nm and a second signal at 265 nm. The experimental data show a first broad signal centred at ≈340 nm with a small shoulder at almost 290 nm and a second peak at shorter wavelengths (λ_{max}≈250 nm). In the light of these findings, our computations well reproduce the electronic UV/Vis absorption spectra of **T-VPI-H**$^+$ in water solution; the only thing to mention is that the shoulder revealed in the experiments – previously detected at around 305 nm – actually remains confined within the lowest energy absorption signal. More in details: *i)* the lowest $^1\pi \rightarrow \pi^*$ (HOMO-1 → LUMO) energy band – at QM [CAM-B3LYP(D3)]/6–311+G**)/MM/C-PCM level – samples excitation wavelengths in a spectral region from 330 to 343 nm with an average value of 341 nm and a standard deviation of 5 nm ($0.82 \leq f \leq 1.15$); *ii)* the second excitation results – with respect to the value detected at CAM-B3LYP(D3)/6–311+G**)/C-PCM level of 302 nm – on average red shifted by almost 12 nm ($0.40 \leq f \leq 0.53$); *iii)* the third excitation responsible for the $^1\pi \rightarrow \pi^*$ band at 265 nm shows excitation wavelengths with an average value of 264 nm and a standard deviation of 3 nm ($0.71 \leq f \leq 0.84$); *iiii)* water molecules treated at QM level in the proposed adaptive QM/MM scheme are those encircling the two amine-hydrogen moieties of the **I**midazole unit. In this respect, the inset reported in Fig. 5b clearly highlights the oxygen water orientation – with a maximum of 4 different solvent molecules – forming the prominent O_W–H-N(**I**) electrostatic interactions along the explored time range (400 ns at 298 K) under acidic conditions. The remaining solvent molecules forming the nanodroplets perturb the investigated molecular thread by means of both explicit (via an atomic point charge distribution which follows the trajectory that has emerged from the adopted MD sampling) and implicit (C-PCM) solvation models. Finally, we would like to underline that the applied computational approach is methodologically close to those in which nanosolvation patterns at the solute/solvent interface are finely investigated using a QM picture approximating Born–Oppenheimer (BO) surfaces. In this respect, this contribution is substantially based on a classical MD sampling which – although with the due approximations – allows to extend the sampling over hundreds of nanoseconds. As conclusive remark, an effective intramolecular charge transfer (ICT) [50] along the sampling from electron donating group to the electron accepting group – like for example from the **I**midazole subunit to the remaining molecular skeleton in **TVPI**, see Fig. 3 – appears to be rather improbable since the fluctuating HOMO-LUMO energy gap is systematically found at value larger than 4.77 eV (**TVPI**) and 5.25 eV (**TVPI-H**$^+$).

4. Conclusions

In this contribution we report a computational study focused on a recently proposed artificial molecular thread in water dilute solution in neutral and acidic conditions. At first, we have characterized the electronic degrees of freedom involved in the electronic excitation patterns via a TD-DFT/C-PCM approach. These computations let us suppose the existence of intermoieties charge-transfer processes capable of modulating the interaction with UV/Vis light pulses in aqueous environment. These spectroscopic observables are also further investigated within a self-consistent and adaptive QM/MM/C-PCM partitioning scheme within spherical nanodroplets in the presence of thermal effects. The derived UV/Vis absorption spectra for both **T-VPI** and **T-VPI-H**$^+$ species agree with recent experimental measurements acquired in water dilute solution at 298 K. In addition, Conceptual DFT descriptors analytically identify the nitrogen atom of the **I**midazole moiety as the most preferred site for an electrophilic attack. After all, this trend meets the experimental observations showing that the acidification of the solution brings to the formation of **T-VPI-H**$^+$ molecular thread. In conclusion, we are confident that the present contribution might shed some light on the importance of perturbing solvation effects on the electronic properties of such an intriguing synthetic molecular thread.

CRediT authorship contribution statement

Costantino Zazza: Writing – original draft, Visualization, Software, Methodology, Investigation, Data curation. **Nico Sanna:** Visualization, Supervision, Project administration. **Stefano Borocci:** Visualization, Supervision, Methodology, Conceptualization. **Felice Grandinetti:** Writing – review & editing, Conceptualization.

Declaration of competing interest

The authors declare that they have no known competing financial interests or personal relationships that could have appeared to influence the work reported in this paper.

Acknowledgements

This study is supported by the Rome Technopole foundation within the PNRR action in the field of the NextGenerationEU - section 4. “Digital, Industry and Aerospace”. We would like to thank the University of Tuscia for having allowed the utilization of the DIBAF Cluster HPC Infrastructure where all the computations were carried out.

Data availability

Data will be made available on request.

References

[1] V. Balzani A. Credi M. Venturi M. Molecular Machines and Devices: Concepts and Perspectives for the Nanoworld; Wiley-VCH 2008 Weinheim, Germany.
[2] R.A.L. Jones, Soft Machines, Nanotechnology and Life; Oxford University Press, Oxford, U.K., 2004.
[3] E.R. Kay, D.A. Leigh, F. Zerbetto, Synthetic Molecular Motors and Mechanical Machines, Angew. Chem., Int. Ed. 46 (2006) 72–191, https://doi.org/10.1002/anie.200504313.
[4] V. Balzani, A. Credi, M. Venturi, Molecular Devices and Machines, NanoToday 2, (2007), 18–25 and quoted references therein cited. https://doi.org/10.1016/S1748-0132(07)70055-5.
[5] S. Saha, J.F. Stoddart, Photo-Driven Molecular Devices, Chem. Soc. Rev. 36 (2007) 77–92, https://doi.org/10.1039/B607187B.
[6] A. Livoreil, C.O. Dietrich-Buchecker, J.-P. Sauvage, Electrochemically Triggered Swinging of a [2]-Catenate, J. Am. Chem. Soc. 116 (1994) 9399, https://doi.org/10.1021/ja00099a095.
[7] L. Fang, M.A. Olson, D. Benítez, E. Tkatchouk, W.A. Goddard III, J.F. Stoddart, Mechanically Bonded Macromolecules, Chem. Soc. Rev. 39 (2010) 17–29, https://doi.org/10.1039/B917901A.
[8] J.F. Stoddart, Molecular Machines, Acc. Chem. Res. 34 (2001) 410–411, https://doi.org/10.1021/ar010084w.
[9] M. Schliwa, G. Woehlke, Molecular Motors, Nature 422 (2003) 759–765, https://doi.org/10.1038/nature01601.

[10] J. Squire, D. Parry, Fibrous Protein: Muscle and Molecular Motors; Advances in Protein Chemistry Series, vol. 71, Academic Press, San Diego, 2005.
[11] H. Hess, G.D. Bachand, Biomolecular motors, Nanotoday 8 (2005) 22, https://doi.org/10.1016/S1369-7021(05)71286-4.
[12] R.K. Nakamoto, J.A. Baylis Scanlon, M.K. Al-Shawi, The rotary mechanism of the ATP synthase, Arch Biochem Biophys. 476(2008) 43-50. https://doi:10.1016/j.abb.2008.05.004.
[13] O. Mayans, P.F. van der Ven, M. Wilm, A. Mues, P. Young, D.O. Fürst, M. Wilmanns, M. Gautel, The structural basis of the activation mechanism of the serine kinase domain of the giant muscle protein titin during myofibrillogenesis, Nature 395 (1998) 863, https://doi.org/10.1038/27603.
[14] S. Lv, D.M. Dudek, Y. Cao, M.M. Balamurali, J. Gosline, H. Li, Designed biomaterials to mimic the mechanical properties of muscles, Nature 465 (2010) 69, https://doi.org/10.1038/nature09024.
[15] S. Watanabe, K. Mabuchi, R. Ikebe, M. Ikebe, Mechanoenzymatic characterization of human myosin Vb, Biochem. 45 (2006) 2729, https://doi.org/10.1021/bi051682b.
[16] G. Piazzesi, M. Reconditi, M. Linari, L. Lucii, V. Lombardi, Mechanism of force generation by myosin heads in skeletal muscle, Nature 415 (2002) 659–662, https://doi.org/10.1038/415659a.
[17] M. Caremani, M. Marcello, I. Morotti, et al., The force of the myosin motor sets cooperativity in thin filament activation of skeletal muscles, Commun Biol 5 (2022) 1266, https://doi.org/10.1038/s42003-022-04184-0.
[18] G. Ragazzon, M. Baroncini, S. Silvi, M. Venturi, A. Credi, Light-Powered Autonomous and Directional Molecular Motion of a Dissipative Self-Assembling System Nature Nanotech. 10 (2014) 70–75, https://doi.org/10.1038/nnano.2014.260.
[19] C. Zazza, S. Borocci, N. Sanna, A theoretical study of a light-powered artificial molecular motor in dichloromethane solution under equilibrium conditions, Chem. Phys. Lett. 829 (2023) 140758, https://doi.org/10.1016/j.cplett.2023.140758.
[20] P. Roy, W.R. Browne, B.L. Feringa, S.R. Meech, Ultrafast motion in a third generation photomolecular motor, Nat Commun 14 (2023) 1253, https://doi.org/10.1038/s41467-023-36777-6.
[21] C. Zazza, S. Borocci, N. Sanna, A computational study of a light-driven artificial device: a third generation rotational photo-molecular motor in dilute solutions, Phys. Chem. Chem. Phys. 26 (2024) 5399–5407, https://doi.org/10.1039/D3CP05116A.
[22] K. Kuntze, D.R.S. Pooler, M. Di Donato, M.F. Hilbers, P. Van Der Mulen, W. J. Buma, A. Priimagi, B. Feringa, S. Crespi, A visible-light-driven molecular motor based on barbituric acid, Chem. Sci. 14 (2023) 8458–8465, https://doi.org/10.1039/D3SC03090C.
[23] C. Zazza, N. Sanna, S. Borocci, F. Grandinetti, On the conformational shaping of a visible light-driven molecular motor based on barbituric acid in solvents of increasing polarity, Chem. Phys. Lett. 842 (2024) 141205, https://doi.org/10.1016/j.cplett.2024.141205.
[24] D.-H. Qu, B. Feringa, Controlling Molecular Rotary Motion with a Self-Complexing Lock, Angew. Chem., Int. Ed. 49 (2010) 1107–1110, https://doi.org/10.1002/anie.200906064.
[25] C. Zazza, G. Mancini, G. Brancato, V. Barone, In Silico Study of Molecular-Engineered Nanodevices: A Lockable Light-Driven Motor in Dichloromethane Solution, J. Phys. Chem. Letters 4 (2013) 3885–3890, https://doi.org/10.1021/jz4019404.
[26] A. Kriat, S. Pascal, B. Kauffmann, Y. Ferrand, D. Bergé-Lefranc, D. Gigmes, O. Siri, A. Kermagoret, D. Bardelang, A pH- and Metal-Actuated Molecular Shuttle in Water, Chem. Eur. J. 29 (2023) e202300633.
[27] C. Zazza, N. Sanna, S. Borocci, F. Grandinetti, On the supramolecular interactions into a pH- and Metal-Actuated Molecular Shuttle: some insights from QTAIM modelling, ChemPhysChem (2024) e202400603.
[28] W. Koch, M.C. Holthausen, A Chemist's Guide to Density Functional Theory, Wiley-VCH Verlag GmbH (2001), https://doi.org/10.1002/3527600043.
[29] A.D. Becke, Density-functional exchange-energy approximation with correct asymptotic behavior, Phys. Rev. A 38 (1988) 3098, https://doi.org/10.1103/PhysRevA.38.3098.
[30] C. Lee, W. Yang, R.G. Parr, Development of the Colle-Salvetti correlation-energy formula into a functional of the electron density, Phys. Rev. B 37 (1988) 785, https://doi.org/10.1103/PhysRevB.37.785.
[31] S.H. Vosko, L. Wilk, M. Nusair, Accurate spin-dependent electron liquid correlation energies for local spin density calculations: a critical analysis, Can. J. Phys. 58 (1980) 1200, https://doi.org/10.1139/p80-159.
[32] T. Yanai, D. Tew, N. Handy, A new hybrid exchange-correlation functional using the Coulomb-attenuating method (CAM-B3LYP), Chem. Phys. Lett. 393 (2004) 51–57, https://doi.org/10.1016/j.cplett.2004.06.011.
[33] C. Adamo, V. Barone, Toward reliable density functional methods without adjustable parameters: The PBE0 model, J. Chem. Phys. 110 (1999) 6158, https://doi.org/10.1063/1.478522.
[34] Dunning, T.H., Hay, P.J. Gaussian Basis Sets for Molecular Calculations. In: Schaefer, H.F. (eds) Methods of Electronic Structure Theory. Modern Theoretical Chemistry, vol 3. Springer, Boston, MA, 1977. https://doi.org/10.1007/978-1-4757-0887-5_1.
[35] S. Grimme, J. Antony, S. Ehrlich, H. Krieg, A consistent and accurate ab-initio parameterization of density functional dispersion correction (DFT-D) for the 94 elements H-Pu, J. Chem. Phys. 132 (2010) 154104, https://doi.org/10.1063/1.3382344.
[36] P. Pulay, G. Fogarasi, Geometry optimization in redundant internal coordinates, J. Chem. Phys. 96 (1992) 2856–2860, https://doi.org/10.1063/1.462844.
[37] M. Cossi, N. Rega, G. Scalmani, V. Barone, Energies, Structures, and electronic Properties of Molecules in Solution with the C-PCM Solvation Model, J. Comput. Chem. 24 (2003) 669–681, https://doi.org/10.1002/jcc.10189.
[38] Gaussian 16, Revision C.01, M. J. Frisch, G. W. Trucks, H. B. Schlegel, G. E. Scuseria, M. A. Robb, J. R. Cheeseman, G. Scalmani, V. Barone, G. A. Petersson, H. Nakatsuji, X. Li, M. Caricato, A. V. Marenich, J. Bloino, B. G. Janesko, R. Gomperts, B. Mennucci, H. P. Hratchian, J. V. Ortiz, A. F. Izmaylov, J. L. Sonnenberg, D. Williams-Young, F. Ding, F. Lipparini, F. Egidi, J. Goings, B. Peng, A. Petrone, T. Henderson, D. Ranasinghe, V. G. Zakrzewski, J. Gao, N. Rega, G. Zheng, W. Liang, M. Hada, M. Ehara, K. Toyota, R. Fukuda, J. Hasegawa, M. Ishida, T. Nakajima, Y. Honda, O. Kitao, H. Nakai, T. Vreven, K. Throssell, J. A. Montgomery, Jr., J. E. Peralta, F. Ogliaro, M. J. Bearpark, J. J. Heyd, E. N. Brothers, K. N. Kudin, V. N. Staroverov, T. A. Keith, R. Kobayashi, J. Normand, K. Raghavachari, A. P. Rendell, J. C. Burant, S. S. Iyengar, J. Tomasi, M. Cossi, J. M. Millam, M. Klene, C. Adamo, R. Cammi, J. W. Ochterski, R. L. Martin, K. Morokuma, O. Farkas, J. B. Foresman, and D. J. Fox, Gaussian, Inc., Wallingford CT, 2016.
[39] P. Geerlings, F. De Proft, W. Langenaeker, Conceptual Density Functional Theory, Chem. Rev. 103 (2003) 1793–1874, https://doi.org/10.1021/cr990029p.
[40] R. Pino-Rios, O. Yañez, D. Inostroza, L. Ruiz, C. Cardenas, P. Fuentealba, W. Tiznado, Proposal of a simple and effective local reactivity descriptor through a topological analysis of an orbital-weighted fukui function, J. Comput, Chem. 38 (2017) 481–488, https://doi.org/10.1002/jcc.24699.
[41] T. Lu, F. Chen, Multiwfn: A multifunctional wavefunction analyser, J. Comput. Chem. 33 (2012) 580–592, https://doi.org/10.1002/jcc.22885.
[42] R.E. Stratmann, G.E. Scuseria, M.J. Frisch, An efficient implementation of time-dependent density-functional theory for the calculation of excitation energies of large molecules, J. Chem. Phys. 109 (1998) 8218–8224, https://doi.org/10.1063/1.477483.
[43] H.J. Berendsen, J.R. Grigera, T.P. Straatsma, The missing term in effective pair potentials, J. Phys. Chem. 91 (1987) 6269–6271. https://doi:10.1021/j100308a038.
[44] W.L. Jorgensen, D.S. Maxwell, J. Tirado-Rives, Development and Testing of the OPLS All-Atom Force Field on Conformational Energetics and Properties of Organic Liquids, J. Am. Chem. Soc. 118 (1996) 11225–11236, https://doi.org/10.1021/ja9621760.
[45] D. Van Der Spoel, E. Lindahl, B. Hess, G. Groenhof, A.E. Mark, H.J.C. Berendsen, GROMACS: Fast, flexible, and free, J. Comput. Chem. 26 (2005) 1701–1718, https://doi.org/10.1002/jcc.20291.
[46] J. Stare, J. Mavri, J. Grdadolnik, J. Zidar, Z.B. Maksić, R. Vianello, Hydrogen Bond Dynamics of Histamine Monocation in Aqueous Solution: Car-Parrinello Molecular Dynamics and Vibrational Spectroscopy Study, J. Phys. Chem. B 115 (2011) 5999–6010, https://doi.org/10.1021/jp111175e.
[47] R. Vianello, J. Mavri, Microsolvation of the histamine monocation in aqueous solution: the effect on structure, hydrogen bonding ability and vibrational spectrum, New J. Chem. 36 (2012) 954–962, https://doi.org/10.1039/c2nj20877f.
[48] D. Borgis, G. Tarjus, H. Azzouz, An adiabatic dynamical simulation study of the Zundel polarization of strongly H-bonded complexes in solution, J. Chem. Phys. 97 (1992) 1390–1400, https://doi.org/10.1063/1.463265.
[49] H.-S. Andrei, N. Solc, O. Dopfer, Microhydration of Protonated Biomolecular BuildingBlocks: IR Spectra of Protonated Imidazole– $Water_n$ Complexes, ChemPhysChem 7 (2006) 107–110, https://doi.org/10.1002/cphc.200500432.
[50] R.A. Markus, Electron Transfer Reactions in Chemistry: Theory and Experiment (Nobel Lecture), Angew. Chem. 32 (1993) 1111–1221, https://doi.org/10.1002/anie.199311113.